J. Mech. Phys. Solids 164 (2022) 104918

Contents lists available at ScienceDirect

Journal of the Mechanics and Physics of Solids

journal homepage: www.elsevier.com/locate/jmps

Active filaments I: Curvature and torsion generation

Bartosz Kaczmarski [b,1], Derek E. Moulton [a,1], Ellen Kuhl [b,1], Alain Goriely [a,1,*]

[a] Mathematical Institute, University of Oxford, United Kingdom
[b] Living Matter Laboratory, Stanford University, Stanford, CA, USA

ARTICLE INFO

Keywords:
Rods
Filaments
Elasticity
Anelasticity
Dimensional reduction

ABSTRACT

In many filamentary structures, such as hydrostatic arms, roots, and stems, the active or growing part of the material depends on contractile or elongating fibers. Through their activation by muscular contraction or growth, these fibers will generate internal stresses that are partially relieved by the filament acquiring intrinsic torsion and curvature. This process is fundamental in morphogenesis but also in plant tropism, nematic solid activation, and muscular motion of filamentary organs such as elephant trunks and octopus arms. Here, we provide a general theory that links the activation of arbitrary fibers at the microscale to the generation of curvature and torsion at the macroscale. This theory is obtained by dimensional reduction from the full anelastic description of three-dimensional bodies to morphoelastic Kirchhoff rods. Hence, it links the geometry and material properties of embedded fibers to the shape and stiffness of the rod. The theory is applied to fibers that are wound helically around a central core in tapered and untapered filaments.

1. Introduction

Filaments are soft slender mechanical structures that are roughly defined by having one dimension much larger than the typical scale of their cross section. Around us, filaments are the strings, ropes, strands, wires, cables, and cords that we encounter in our daily lives. In mechanics, they include beams, strings, strips, ribbons, and rods (Antman, 2005). *Passive filaments* have fixed material and geometric properties such as length, girth, intrinsic shape, and rigidity. The central problem in the mechanics of these passive objects is to obtain their shapes for given boundary conditions, body forces, and external loads. Due to their particular aspect ratio, the shape of such objects can be captured from their central axis and modeled using a combination of differential geometry of curves and physical balance laws for forces and moments, leading ultimately to the *Kirchhoff equations* of rod theory (Kirchhoff, 1859; Dill, 1992; Goriely and Tabor, 2000). These equations have been successfully applied to structures as varied in size and functions as DNA, proteins (Benham, 1979; Hoffman et al., 2003; Beveridge et al., 2004; Neukirch et al., 2008a,b), polymers and liquid crystals (Sheley and Ueda, 2000), whips and lassos (McMillen and Goriely, 2002; Brun et al., 2014), and bridge cables (Costello, 1990; Yokota et al., 2001).

By contrast, *active filaments* share the same slender geometry but have the additional feature of allowing internal remodeling. Many examples of such active structures can be found in the natural world (Goriely, 2017) including neurons (Oliveri et al., 2021), anguilliform swimmers (McMillen and Holmes, 2006), roots (Moulton et al., 2020b), stems (Goriely and Neukirch, 2006), tendrils (Goriely and Tabor, 1998), trees (Greenhill, 1881; Guillon et al., 2011), seed pods (Hofhuis et al., 2016), and various tentacles (Kier and Smith, 1985; Kier, 2012; Levinson and Segev, 2010; Shoshani, 1998; Wilson et al., 1991; Moulton et al., 2016).

* Corresponding author.
E-mail address: goriely@maths.ox.ac.uk (A. Goriely).
[1] All authors have contributed equally to this work.

https://doi.org/10.1016/j.jmps.2022.104918
Received 28 December 2021; Received in revised form 2 April 2022; Accepted 1 May 2022
Available online 10 May 2022

In the engineering world, it includes some soft robotic arms (Calisti et al., 2011; Hannan and Walker, 2003; Laschi et al., 2012; Paley and Wereley, 2021; Walker et al., 2005; Jones et al., 2021), liquid crystal elastomers (Goriely et al., 2022) and actuators (de Payrebrune and O'Reilly, 2016; Sano et al., 2021). Internal remodeling can be generated by external fields as in the case of magnetic actuation, by growth during morphogenesis, or by muscular contraction. In most situations, the internal changes can be modeled by the relative change of internal geometry of a volume element along a principal direction. Since the activation is done in a single distinguished direction, we refer to such a volume element as a *fiber*, and the activation direction as the *fiber direction*, as shown in Fig. 1. There are now two main questions: What is the intrinsic shape of the filament, for a given activation field, in the absence of body forces and boundary loads? And, what is the shape of the filament when loaded given this intrinsic shape? Here, we will focus on the first question to obtain the *active filament formula* linking fiber activation to intrinsic curvature and torsion.

Our starting point is the general theory developed in Moulton et al. (2020a) for the problem of determining the curvature, extension, and torsion of a filament for an arbitrary anelastic field. Accordingly, we treat the filament as a morphoelastic solid. This is a continuum that can grow, remodel, support stresses and can be subject to large deformations (Goldstein and Goriely, 2006; Goriely and Moulton, 2010; Goriely, 2017). We use the theory of morphoelasticity, which represents deformations due to elasticity, growth, and remodeling through a multiplicative decomposition of the deformation gradient into elastic and growth tensors (Goriely, 2017). In the present work, the decomposition is naturally extended to include the activation process, such as mass-preserving contraction or elongation, in the growth tensor. The problem is then to obtain from the specification of a growth tensor representing fiber activation for the full three dimensional problem, the corresponding reduced one-dimensional morphoelastic rod as defined in Lessinnes et al. (2017), Moulton et al. (2012).

2. General set-up

We briefly recall the basic assumptions from Moulton et al. (2020a). We assume that the filament is a three-dimensional tubular body that is allowed to grow and whose shape varies slowly along its axis. The initial structure is stress-free and growth or anelastic activation is defined at every point as a local change of a volume element. Following the procedure in Moulton et al. (2020a), we define a growth tensor, characterizing at each point the local change of shape of a volume element by the addition, removal, or redistribution of mass. We assume that this filamentary structure deforms into another tubular structure defined by variations along a deformed centerline. The slenderness of this structure introduces naturally a small parameter ε in the problem that can be used to asymptotically expand the energy of the system. This energy can then be minimized, and the stresses and strains within the section can be obtained explicitly, leaving an energy that can be identified with the energy of a rod. This type of dimensional reduction is related to a large body of work in rational mechanics focused on obtaining systematically reduced models from three-dimensional elasticity (Cimetière et al., 1988; Sanchez-Hubert and Palencia, 1999) and anelasticity (Mora and Müller, 2003; Audoly and Lestringant, 2021; Kohn and O'Brien, 2018; Cicalese et al., 2017; Bauer et al., 2019; Kupferman and Solomon, 2014). The emphasis here is not in justifying the reduction but using it to explore the possible shapes that can be created through simple and universal filamentary structures.

2.1. The growth tensor for activation

We consider an initial elastic *tubular* configuration $\mathcal{B}_0 \subset \mathbb{R}^3$ with material points $(X, Y, Z) \in \mathcal{B}_0$ that can be decomposed as the product $[0, L] \times S$ of a segment of the Z-axis between 0 and L and a family of cross-sections S_Z whose centroids are on the Z-axis and oriented with the condition

$$\int_{S_Z} EX \,\mathrm{d}X\mathrm{d}Y = \int_{S_Z} EY \,\mathrm{d}X\mathrm{d}Y = \int_{S_Z} EXY \,\mathrm{d}X\mathrm{d}Y = 0, \tag{1}$$

where E is the Young's modulus. The typical length scale of each section is $\mathcal{O}(\varepsilon)$, corresponding to a typical or averaged radius, and each cross section is a slowly varying function of the arc length Z, so that, on short scales, the tubular structure is cylindrical.

We consider the deformation $\chi(\mathbf{X}) : \mathcal{B}_0 \to \mathcal{B}$ from the initial configuration $\mathcal{B}_0$ to the current configuration $\mathcal{B}$ and model the growth or activation through a tensor $\mathbf{G}$ so that

$$\mathbf{F} = \mathrm{Grad}\, \chi = \mathbf{A}\mathbf{G}, \tag{2}$$

where the gradient is taken with respect to the $\mathbf{X}$ coordinates and $\mathbf{A}$ is an elastic tensor describing the elastic stretches related to a strain–energy density function $W = W(\mathbf{A})$. The tensor $\mathbf{G}$ is given with a strictly positive determinant. In the case of fiber activation, the determinant is governed by the Poisson effect of the activating element. In the general description of growth mechanics, the determinant is larger than 1 for growth, and smaller than 1 for shrinkage. For the rest of the paper, we refer to any process with $\mathbf{G} \neq \mathbf{1}$ as *activation*. Activation is naturally expressed as a map from the cylindrical coordinates $(\varepsilon R, \Theta, Z)$ of the reference configuration to the cylindrical coordinates (r, θ, z) of the current configuration

$$\mathbf{G} = (\mathbf{1} + \mathbf{G}_1)\mathbf{G}_0 = G_{ij}\, \mathbf{e}_i \otimes \mathbf{e}_j, \qquad i \in \{r, \theta, z\},\ j \in \{R, \Theta, Z\}. \tag{3}$$

where $(\mathbf{e}_r, \mathbf{e}_\theta, \mathbf{e}_z)$ and $(\mathbf{e}_R, \mathbf{e}_\Theta, \mathbf{e}_Z)$ are the usual unit cylindrical basis vectors in the current and reference configuration, respectively, and $G_{ij} = G_{ij}(\varepsilon R, \Theta, Z)$. We restrict our analysis to growth tensors that are small deviations with respect to identity, where the deviation is measured with respect to the small parameter ε:

$$\mathbf{G} = \mathbf{1} + \varepsilon \mathbf{G}_0(\mathbf{X}). \tag{4}$$

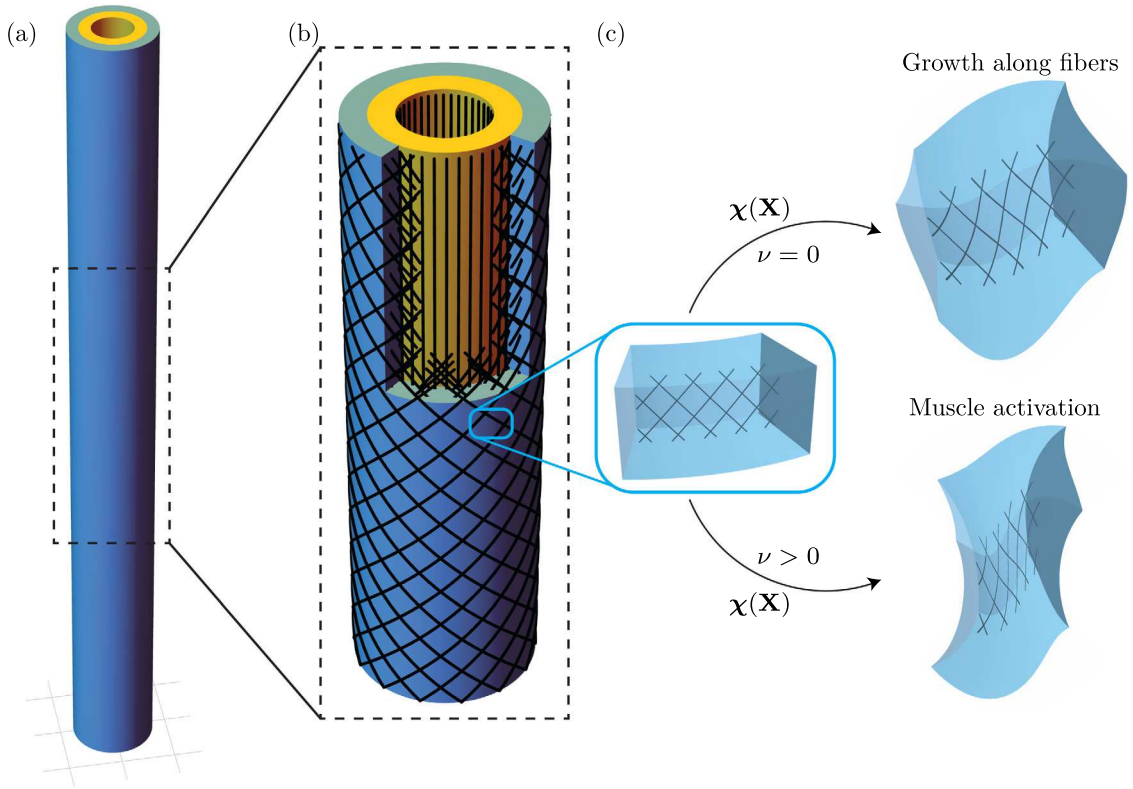

Fig. 1. (a), (b) A filamentary structure that contains a field of fibers embedded throughout its body. (c) An infinitesimal volume element with embedded fibers can deform either through growth along the fibers (with $\det(\mathbf{G}) \neq 1$ and $\nu = 0$) or through muscle activation (with $\nu \in [0, 1/2]$ — see text), in which case no new material is produced in the filament body, and the change in size in the directions perpendicular to the activating fiber is due to the Poisson effect with Poisson's ratio ν.

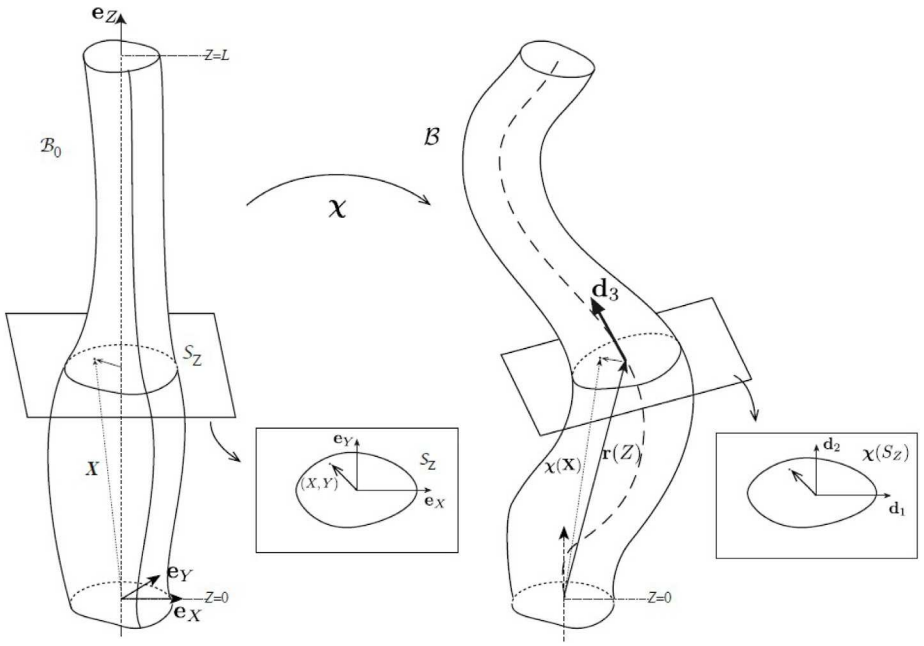

Fig. 2. We consider a tubular structure in the reference configuration (left) and its deformation in the current configuration (right). The deformed configuration is fully parameterized by the centerline $\mathbf{r}(Z)$ and the deformation of each cross section.

A key assumption of our theory is that we restrict our attention to a particular family of possible deformations, mapping a straight tubular structure to a filament in space $\mathcal{B}$ with centerline $\mathbf{r}(Z)$ as shown in Fig. 2. This centerline is the image of a segment of the Z-axis defining the centerline of the initial configuration. From this centerline, we define a local director basis $(\mathbf{d}_1(Z), \mathbf{d}_2(Z), \mathbf{d}_3(Z))$ where $\mathbf{r}'(Z) = \zeta \mathbf{d}_3$, ζ is the axial extension, and $(\,)'$ denotes derivatives with respect to the material coordinate Z. From the director basis, we define the Darboux curvature vector $\mathbf{u} = \mathrm{u}_1\mathbf{d}_1 + \mathrm{u}_2\mathbf{d}_2 + \mathrm{u}_3\mathbf{d}_3$. This vector describes the evolution of the director basis along the filament, satisfying

$$\mathbf{d}_i'(Z) = \zeta \mathbf{u} \times \mathbf{d}_i. \tag{5}$$

The mapping $\chi : \mathcal{B}_0 \to \mathcal{B}$ is then written

$$\chi(\mathbf{X}) = \mathbf{r}(Z) + \sum_{i=1}^{3} \varepsilon a_i(\varepsilon R, \Theta, Z)\mathbf{d}_i(Z), \tag{6}$$

where the *reactive strains* a_i correspond to deformations of the sections and are to be determined; these satisfy $a_i(0,0,Z) = 0$ so that the Z-axis maps to the centerline $\mathbf{r}(Z)$. The particular form (6) expresses the deformation of a tubular body in terms of its centerline and director basis. We note that, since the section has a typical radius ε, the variable R is an order 1 quantity. Taking $\zeta = 1 + \varepsilon\xi$, the deformation gradient $\mathbf{F} = F_{ij}\mathbf{d}_i \otimes \mathbf{e}_j, i \in \{1,2,3\}, j \in \{R, \Theta, Z\}$ is then given by

$$\mathbf{F} = \begin{bmatrix} a_{1R} & \frac{1}{R}a_{1\Theta} & \varepsilon(1+\varepsilon\xi)\left(\mathrm{u}_2 a_3 - \mathrm{u}_3 a_2\right) \\ a_{2R} & \frac{1}{R}a_{2\Theta} & \varepsilon(1+\varepsilon\xi)\left(\mathrm{u}_3 a_1 - \mathrm{u}_1 a_3\right) \\ a_{3R} & \frac{1}{R}a_{3\Theta} & (1+\varepsilon\xi)\left(1+\varepsilon(\mathrm{u}_1 a_2 - \mathrm{u}_2 a_1)\right) \end{bmatrix}. \tag{7}$$

Next, we consider a continuum with a distinguished direction that we call a *fiber*. Whereas we utilize a model for a material containing fibers that can be activated, it is worth noting that, in our model, the material does not actually contain physical fibers within a matrix. Rather, we assume that the density of fibers is large enough so that they can be represented, locally, by a vector field $\mathbf{m}$, as shown in Fig. 3. In cylindrical coordinates, this arbitrary fiber direction $\mathbf{m}$ is described by two angles α and β:

$$\mathbf{m} = \sin\alpha \sin\beta\ \mathbf{e}_R + \sin\alpha\cos\beta\ \mathbf{e}_\Theta + \cos\alpha\ \mathbf{e}_Z, \quad \alpha, \beta \in [-\pi/2, \pi/2]. \tag{8}$$

Helical fibers are tangent to a cylinder centered around the axis and are therefore prescribed by $\beta = 0$ and $\alpha \in [-\pi/2, \pi/2]$ with limiting cases of a *hoop fiber* at $\alpha = +\pi/2$ and an *axial fiber* at $\alpha = 0$. A *right-handed helical fiber* is given by $0 < \alpha < \pi/2$ and a *left-handed helical fiber* is specified by $-\pi/2 < \alpha < 0$. *Sectional fibers* lie in the cross-section and are characterized by $\alpha = \pi/2$, with *radial fibers* given by $\beta = \pi/2$ and, in the limit $\beta = 0$, we recover hoop fibers, as before.

Since we are only considering elongation or contraction along this fiber, $\mathbf{m}$ must be an eigenvector of the tensor $\mathbf{G}$ with eigenvalue g. Similarly, the perpendicular vector $\mathbf{m}_\perp = \cos\beta\ \mathbf{e}_R - \sin\beta\ \mathbf{e}_\Theta$ and $\mathbf{m}_\perp' = \mathbf{m} \times \mathbf{m}_\perp$ are also eigenvectors of $\mathbf{G}$:

$$\mathbf{G}\cdot\mathbf{m} = \delta\mathbf{m}, \quad \mathbf{G}\cdot\mathbf{m}_\perp = \delta_\perp\mathbf{m}_\perp, \quad \mathbf{G}\cdot\mathbf{m}_\perp' = \delta_\perp'\mathbf{m}_\perp'. \tag{9}$$

We consider two cases: growth and activation (see Fig. 1c). In the growth case, there is a change of length of the fiber $\delta = 1 + \varepsilon g(R,\Theta)$ that is not accompanied by a change in the transverse direction and $\delta_\perp = \delta_\perp' = 1$. For active fibers, the extension (contraction) of the fiber generates a contraction (extension) in the transverse directions, with any change in volume due to the action of $\mathbf{G}$ described by the Poisson's ratio. Therefore, for small ϵ, we have $\delta_\perp = \delta_\perp' = 1 - \varepsilon\nu g(R,\Theta)$ and $\delta = 1 + \varepsilon g(R,\Theta)$, where ν is the Poisson's ratio. We see that both cases can be combined by taking either $\nu = 0$ for growth and $\nu \in [0, 1/2]$ for an active fiber (in the case $\nu = 0$, there is no distinction between an active fiber and growth as the material extends without lateral contraction). We emphasize that α, β and g may be functions of R, Θ, and, possibly, slowly varying functions of Z. Combining both cases, the growth tensor in cylindrical coordinates is

$$\mathbf{G} = \mathbf{1} + \varepsilon g \begin{bmatrix} (1+\nu)\sin^2\alpha\sin^2\beta - \nu & (1+\nu)\sin^2\alpha\sin\beta\cos\beta & (1+\nu)\sin\alpha\cos\alpha\sin\beta \\ (1+\nu)\sin^2\alpha\sin\beta\cos\beta & -(1+\nu)\sin^2\alpha\sin^2\beta - \nu & (1+\nu)\sin\alpha\cos\alpha\cos\beta \\ (1+\nu)\sin\alpha\cos\alpha\sin\beta & (1+\nu)\sin\alpha\cos\alpha\cos\beta & \frac{1}{2}(1-\nu+(1+\nu)\cos 2\alpha) \end{bmatrix}. \tag{10}$$

2.2. The energy density

We assume that the growing material is a compressible hyperelastic material with strain–energy density $W = W(\mathbf{A})$. The total energy of the system is

$$\mathcal{W} = \int_{\mathcal{B}_0} W(\mathbf{A})\det\mathbf{G}\,\mathrm{d}X\mathrm{d}Y\mathrm{d}Z, \tag{11}$$

which can be written in terms of $\mathbf{F}$ and $\mathbf{G}$ as

$$\mathcal{W} = \int_{\mathcal{B}_0} V(\mathbf{F}\mathbf{G}^{-1}, \mathbf{G})\mathrm{d}X\mathrm{d}Y\mathrm{d}Z, \qquad V = W(\mathbf{F}\mathbf{G}^{-1})\det\mathbf{G}. \tag{12}$$

The problem is then to minimize this energy for a given $\mathbf{G}$ over the set of allowable deformations gradients $\mathbf{F}$ considered above. In cylindrical coordinates, the energy functional can be written

$$\mathcal{W} = \varepsilon^2 \int_0^L \mathrm{d}Z \int_S V(\mathbf{F}\mathbf{G}^{-1}, \mathbf{G})\, R\,\mathrm{d}R\mathrm{d}\Theta. \tag{13}$$

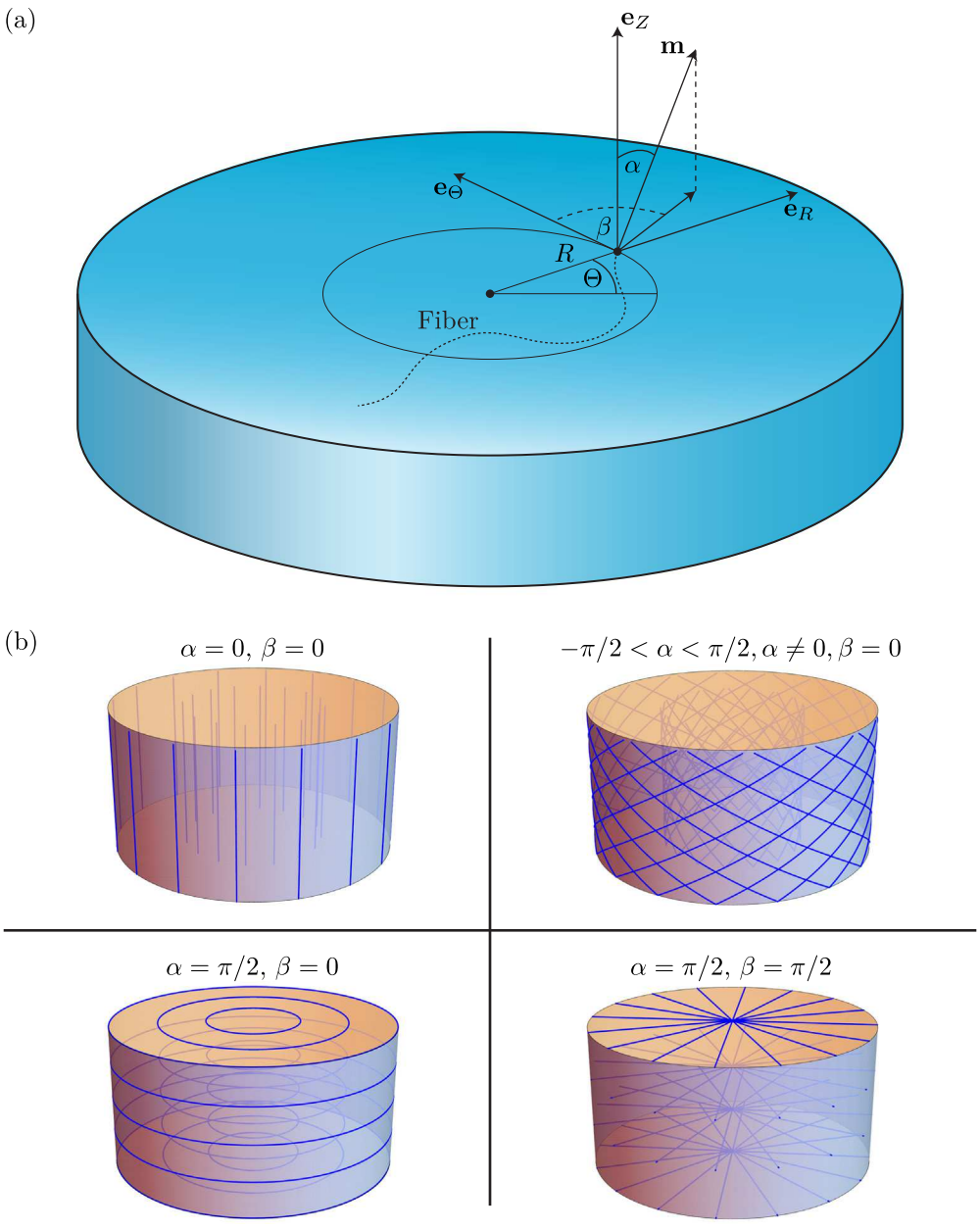

Fig. 3. (a) We consider arbitrary fibers characterized by angles $\alpha = \alpha(R, \Theta)$ and $\beta = \beta(R, \Theta)$ with respect to the section. (b) Representative fiber architectures for constant α and β: axial (top-left), helical (top-right), hoop (bottom-left), and radial (bottom-right) fibers.

We proceed by expanding the inner variables a_i, with the auxiliary energy density taking the form

$$V(\mathbf{F}\mathbf{G}^{-1}, \mathbf{G}) = V_0 + \varepsilon^2 V_2 + \mathcal{O}(\varepsilon^3), \tag{14}$$

where each $V_i = V_i(a_1^{(i)}, a_2^{(i)}, a_3^{(i)}, a_{1_R}^{(i)}, a_{2_R}^{(i)}, a_{3_R}^{(i)}, a_{1_\Theta}^{(i)}, a_{2_\Theta}^{(i)}, a_{3_\Theta}^{(i)})$. The Euler–Lagrange equations then become

$$\frac{\partial}{\partial R}\frac{\partial V_i}{\partial a_{jR}^{(k)}} + \frac{1}{R}\frac{\partial V_i}{\partial a_{jR}^{(k)}} + \frac{\partial}{\partial \Theta}\frac{\partial V_i}{\partial a_{j\Theta}^{(k)}} - \frac{\partial V_i}{\partial a_j^{(k)}} = 0, \quad j = 1, 2, 3,\ k = 0, 1, \tag{15}$$

with the appropriate natural boundary conditions.

To lowest order, the solution of the Euler–Lagrange equations is given by

$$\boldsymbol{a}^{(0)} = R(\cos\Theta, \sin\Theta, 0). \tag{16}$$

To order $\mathcal{O}(\varepsilon)$, the Euler–Lagrange equations are identically satisfied. To order $\mathcal{O}(\varepsilon^2)$, the solution for the reactive strains is

$$a_1^{(1)} = -\frac{\lambda R}{4(\lambda+\mu)}\left(R\mathsf{u}_1 \sin 2\theta - R\mathsf{u}_2 \cos 2\theta + 2\xi \cos\theta\right) + f_1(R,\Theta), \tag{17}$$

$$a_2^{(1)} = \frac{\lambda R}{4(\lambda+\mu)}\left(R\mathsf{u}_1 \cos 2\theta + R\mathsf{u}_2 \sin 2\theta - 2\xi \sin\theta\right) + f_2(R,\Theta), \tag{18}$$

$$a_3^{(1)} = \omega(R,\theta) + \mathsf{u}_3\phi(R,\theta), \tag{19}$$

where $f_{1,2}$ are functions that only enter in the so-called *reactive part* of the energy and are not needed to compute the moduli and intrinsic curvature.

The function $\phi(R,\Theta)$ is the classic *warping function* and is a solution of the Neumann problem for the Laplace equation:

$$\Delta\phi = 0, \quad \mathbf{X} \in S \tag{20}$$

$$\mathbf{n}\cdot \mathrm{Grad}\,\phi = -R\,\mathbf{n}.\mathbf{e}_\Theta, \quad \mathbf{X} \in \partial S, \tag{21}$$

where $\mathbf{n}$ is the unit outward normal vector to the cross section boundary ∂S.

The function $\omega(R,\Theta)$ is a new function that we call the *torsion function*. It is given by the solution of the Poisson equation with a null Neumann condition:

$$\begin{aligned}\Delta\omega = -2R(1+\nu)\big[&\sin\alpha\cos\alpha\left(Rg_R\sin\beta + g_\Theta\cos\beta\right) + \\ &g\left(-R\alpha_R\sin^2\alpha\sin\beta + \alpha_\Theta\cos(2\alpha)\cos\beta + R\alpha_R\cos^2\alpha\sin\beta - \right. \\ &\left.\beta_\Theta\sin\alpha\cos\alpha\sin\beta + R\beta_R\sin\alpha\cos\alpha\cos\beta + \sin\alpha\cos\alpha\sin\beta\right)\big]\end{aligned} \tag{22}$$

$$\mathbf{n}\cdot\mathrm{Grad}\,\omega = 0, \quad \mathbf{X} \in \partial S. \tag{23}$$

With the solution for the reactive strains, the energy takes the form

$$\mathcal{E} = \varepsilon^4 \int_0^L \mathrm{d}Z \int_S R\,V_2(\mathbf{a}^{(0)}, \mathbf{a}^{(1)}; \mathsf{u}_1, \mathsf{u}_2, \mathsf{u}_3, \xi)\,\mathrm{d}R\,\mathrm{d}\Theta + \mathcal{O}(\varepsilon^5). \tag{24}$$

Since the strain–energy density is isotropic and its contribution in the expression for V includes at most quadratic terms in the strains, we can use without loss of generality the quadratic approximation of W:

$$W = \frac{1}{2}\left[\mu\left(\mathrm{tr}\left(\mathbf{H}.\mathbf{H}^T\right) + \mathrm{tr}(\mathbf{H}^2)\right) + \lambda\,\mathrm{tr}(\mathbf{H})^2\right], \tag{25}$$

where $\mathbf{H} = \mathbf{A} - \mathbf{1}$ and μ, λ are the Lamé parameters. After integration, up to order $\mathcal{O}(\varepsilon^4)$, we find

$$\mathcal{E} = \frac{1}{2}\int_0^L K_0(\zeta - \hat{\zeta})^2 + K_1(\mathsf{u}_1 - \hat{\mathsf{u}}_1)^2 + K_2(\mathsf{u}_1 - \hat{\mathsf{u}}_2)^2 + K_3(\mathsf{u}_3 - \hat{\mathsf{u}}_3)^2\,\mathrm{d}Z. \tag{26}$$

Here we have used $\xi = (\zeta - 1)/R_0$ where R_0 is the typical scale of the cross section. We recover the classic extensional, bending, and torsional stiffness coefficients of rod theory

$$K_0 = \int_S E R\,\mathrm{d}R\,\mathrm{d}\Theta, \tag{27}$$

$$K_1 = \int_S E R^3 \sin^2\Theta\,\mathrm{d}R\,\mathrm{d}\Theta, \tag{28}$$

$$K_2 = \int_S E R^3 \cos^2\Theta\,\mathrm{d}R\,\mathrm{d}\Theta, \tag{29}$$

$$K_3 = \int_S \mu\left(R^3 + 2R\phi_\Theta + \frac{1}{R}\phi_\Theta^2 + R\phi_R^2\right)\mathrm{d}R\,\mathrm{d}\Theta, \tag{30}$$

where $E = \mu(3\lambda + 2\mu)/(\lambda + \mu)$ is the Young's modulus which can be taken as a function of position. If E and μ are constant, we recover

$$K_0 = E\mathcal{A}, \quad K_1 = EI_1, \quad K_2 = EI_2 \quad K_3 = \mu J, \tag{31}$$

where $\mathcal{A}$ is area of the cross section whereas $I_{1,2}$ are its second moments of area, and J is a parameter that depends only on the cross-sectional shape and the warping function. In addition, we define

$$H_0 = \frac{1}{2}\int_S E(1 - \nu + (1+\nu)\cos 2\alpha)g\,R\,\mathrm{d}R\,\mathrm{d}\Theta, \tag{32}$$

$$H_1 = \frac{1}{2}\int_S E R^2(1 - \nu + (1+\nu)\cos 2\alpha)g\sin\Theta\,\mathrm{d}R\,\mathrm{d}\Theta, \tag{33}$$

$$H_2 = \frac{1}{2}\int_S E R^2(1 - \nu + (1+\nu)\cos 2\alpha)g\cos\Theta\,\mathrm{d}R\,\mathrm{d}\Theta, \tag{34}$$

$$H_3 = \frac{1}{2}\int_S \frac{E}{\nu+1}\Bigg(g(\nu+1)\sin(2\alpha)\left((R^2 + \phi_\Theta)\cos\beta + R\phi_R\sin\beta\right)$$

$$-\frac{\omega_\Theta\left(\phi_\Theta+R^2\right)}{R}-R\omega_R\phi_R\Big)\,\mathrm{d}R\,\mathrm{d}\Theta. \tag{35}$$

From these quantities, we extract the intrinsic extension and curvatures:

$$\hat{\zeta}=1+H_0/K_0,\quad \hat{\mathrm{u}}_1=H_1/K_1,\quad \hat{\mathrm{u}}_2=-H_2/K_2,\quad \hat{\mathrm{u}}_3=H_3/K_3. \tag{36}$$

We refer to the last three sets of definitions for H_i, K_i and $\hat{\mathrm{u}}_i$ as *the active filament formulas* as they describe in a fundamental way how curvatures are related to *internal* stresses induced by growth or activation. These formulas are named in honor of the fundamental *helical spring formulas* obtained by Thomson and Tait that relate the curvatures to *external* stresses (Thomson and Tait, 1867; Goriely et al., 2012).

3. Particular case of a circular cross-section

The expressions above simplify greatly if we consider a circular cross-section of radius R_0. In that case, the stiffnesses K_i have been tabulated for different types of inclusions and the appropriate formulas can be found in textbooks for different profiles of E. For a uniform material with no variations of E, we have:

$$K_0=E\pi R_0^2,\quad K_1=E\frac{\pi R_0^4}{4},\quad K_2=E\frac{\pi R_0^4}{4},\quad K_3=\frac{E}{1+\nu}\frac{\pi R_0^4}{4}. \tag{37}$$

More interestingly, the warping function is identically zero and, since ω is periodic in Θ, it will not contribute. We then obtain an explicit expression in terms of the given functions $g=g(R,\Theta),\alpha=\alpha(R,\Theta),\beta=\beta(R,\Theta)$, and the material parameters ν and E:

$$H_0=\frac{1}{2}\int_0^{R_0}R\,\mathrm{d}R\int_0^{2\pi}Eg(1-\nu+(1+\nu)\cos 2\alpha)\,\mathrm{d}\Theta, \tag{38}$$

$$H_1=\frac{1}{2}\int_0^{R_0}R^2\,\mathrm{d}R\int_0^{2\pi}Eg(1-\nu+(1+\nu)\cos 2\alpha)\sin\Theta\,\mathrm{d}\Theta, \tag{39}$$

$$H_2=\frac{1}{2}\int_0^{R_0}R^2\,\mathrm{d}R\int_0^{2\pi}Eg(1-\nu+(1+\nu)\cos 2\alpha)\cos\Theta\,\mathrm{d}\Theta, \tag{40}$$

$$H_3=\frac{1}{2}\int_0^{R_0}R^2\,\mathrm{d}R\int_0^{2\pi}Eg\cos\beta\sin 2\alpha\,\mathrm{d}\Theta. \tag{41}$$

3.1. Ring solution

We first consider the case of a ring of helical fibers $R\in[R_1,R_2]$ with constant moduli in a cylinder of radius R_0. We further assume that the helical structure is created initially by a uniform twist, and thus it satisfies the relationship

$$\frac{\tan\alpha}{R}=\frac{\tan\alpha_2}{R_2}, \tag{42}$$

where $\alpha_2\in\,]-\pi/2,+\pi/2[$ is the helical angle on the cylinder of radius R_2. Assuming that each cylinder contains physical helical fibers, the activation g on two different sections is related to the angle α_2 such that

$$g(R,\Theta)=\gamma(\Theta-\frac{Z}{R}\tan\alpha)=\gamma(\Theta-\frac{Z}{R_2}\tan\alpha_2). \tag{43}$$

The functions H_i can then be expressed in terms of the first three Fourier coefficients of γ

$$a_0=\frac{1}{\pi}\int_0^{2\pi}\gamma(\theta)\,\mathrm{d}\theta,\quad a_1=\frac{1}{\pi}\int_0^{2\pi}\gamma(\theta)\cos\theta\,\mathrm{d}\theta,\quad b_1=\frac{1}{\pi}\int_0^{2\pi}\gamma(\theta)\sin\theta\,\mathrm{d}\theta, \tag{44}$$

as follows

$$H_0=\frac{E\pi}{2}\delta_0 a_0, \tag{45}$$

$$H_1=-\frac{E\pi}{3}\delta_1 A\sin(\varphi-\frac{Z}{R_2}\tan\alpha_2), \tag{46}$$

$$H_2=\frac{E\pi}{3}\delta_2 A\cos(\varphi-\frac{Z}{R_2}\tan\alpha_2), \tag{47}$$

$$H_3=\frac{E\pi}{2(1+\nu)}\delta_3 a_0, \tag{48}$$

where we defined A and φ through $a_1=A\cos\varphi$, $b_1=-A\sin\varphi$ and

$$\delta_0=(\nu+1)R_2^2\cot^2\alpha_2\log\left(\frac{R_2^2\sec^2\alpha_2}{R_1^2\tan^2\alpha_2+R_2^2}\right)+\nu\left(R_1^2-R_2^2\right), \tag{49}$$

$$\begin{aligned}\delta_1=\delta_2=&\left(R_1-R_2\right)\left(\nu\left(R_1^2+R_2R_1+R_2^2\right)-3(\nu+1)R_2^2\cot^2\alpha_2\right)\\&+3(\nu+1)R_2^3\cot^3\alpha_2\arctan\left(\frac{R_1\tan\alpha_2}{R_2}\right)-3\alpha_2(\nu+1)R_2^3\cot^3\alpha_2,\end{aligned} \tag{50}$$

$$\delta_3 = -(1+\nu)R_2 \cot\alpha_2 \left(R_1^2 - R_2^2 + R_2^2 \cot^2\alpha_2 \log\left(\frac{2R_2^2}{(R_2^2 - R_1^2)\cos 2\alpha_2 + R_1^2 + R_2^2} \right) \right). \tag{51}$$

From these expressions, we compute the intrinsic stretch and curvatures:

$$\hat{\zeta} = 1 + \frac{a_0 \delta_0}{2R_0^2}, \tag{52}$$

$$\hat{u}_1 = -\frac{4A\delta_1}{3R_0^4} \sin(\varphi - \frac{Z}{R_2}\tan\alpha_2), \tag{53}$$

$$\hat{u}_2 = -\frac{4A\delta_2}{3R_0^4} \cos(\varphi - \frac{Z}{R_2}\tan\alpha_2), \tag{54}$$

$$\hat{u}_3 = \frac{2\delta_3}{R_0^4} a_0. \tag{55}$$

These intrinsic curvatures have the familiar form $\hat{\mathbf{u}} = (\hat{\zeta}\hat{\kappa}\sin\hat{\varphi}, \hat{\zeta}\hat{\kappa}\cos\hat{\varphi}, \hat{\zeta}\hat{\tau} + \hat{\varphi}')$ (Goriely, 2017, p. 103) from which we obtain the intrinsic Frenet curvature and torsion:

$$\hat{\kappa} = \frac{4}{3\hat{\zeta}R_0^4} |\delta_1| A, \tag{56}$$

$$\hat{\tau} = \frac{1}{\hat{\zeta}} \left(\frac{\tan\alpha_2}{R_2} + 2\frac{\delta_3 a_0}{R_0^4} \right). \tag{57}$$

Note that we must include the factor $\hat{\zeta}$ here to take into account the change of length in the rod due to activation. A few comments are in order:

- In the case of incompressible activation ($\nu = 1/2$), the factor $(1 - \nu + (1+\nu)\cos 2\alpha)$ that appears in (38)–(40) is $\delta_1 = 1 + 3\cos 2\alpha$. It vanishes at the *magic angle* (Goriely, 2017) given by $\alpha \approx \pm 54.73$ degrees. Therefore, we can design a system with fiber angles close to that particular angle so that $\delta_1 = \delta_2 = 0$. For this system there is no curvature induced by the activation of the fibers (Goriely and Tabor, 2013). The absence of extension is well known in the theory of McKibben actuators. The absence of curvature at that angle seems to be new and unexpected. It will be further analyzed in the next section.
- The contribution to the curvature from activation is specified by the amplitude of the first Fourier components $A = \sqrt{a_1^2 + b_1^2}$. This amplitude can be controlled by a function γ that can be either continuous or discrete.
- The activation of a ring sector with $A\delta_1 \neq 0$ leads in general to an intrinsic helical centerline since both curvature and torsion are constant.
- Right-handed helical fibers can lead to a left-handed helical shape if $-a_0$ is sufficiently large, which requires average *contraction* of the fiber on the ring. Any extension of the fibers will lead to a shape with the same handedness.
- We emphasize again that the contribution of any activation function $\gamma(\theta)$ only enters through its first three Fourier coefficients. Hence, on a ring, there are at most three independent degrees of freedom dictating the curvatures.

3.2. Ring solution with piecewise constant and uniform activation

We further constrain the system by assuming that activation is uniform along Z and piecewise constant along θ, as shown in Fig. 4, and take $R_2 = R_0$. Let $B[x; x_0, \sigma]$ be the real 2π-periodic function that is zero everywhere except in the interval $[x_0 - \sigma/2, x_0 + \sigma/2]$ where it is equal to one. Then, our activation function has N equally spaced helical activators in the ring:

$$\gamma(\theta) = \sum_{i=0}^{N-1} \gamma_{i+1} B[\theta; \theta_0 + \frac{2\pi i}{N}, \sigma], \tag{58}$$

where $\sigma \leq 2\pi/N$ to avoid overlap. The corresponding Fourier coefficients are:

$$a_0 = \frac{\sigma}{\pi} \sum_{i=1}^{N} \gamma_i, \tag{59}$$

$$a_1 = 2\frac{\sin(\sigma/2)}{\pi} \sum_{i=0}^{N-1} \gamma_{i+1} \cos(\theta_0 + \frac{2\pi i}{N}), \tag{60}$$

$$b_1 = 2\frac{\sin(\sigma/2)}{\pi} \sum_{i=0}^{N-1} \gamma_{i+1} \sin(\theta_0 + \frac{2\pi i}{N}). \tag{61}$$

We observe that there are only three independent variables for activation: a_0, a_1, and b_1. Therefore, one does not need more than three independent activators, i.e., the choice $N = 3$ is sufficient in terms of their relative effect, and their angular extent can be adjusted to increase the magnitude of the response. The variable θ_0 is a phase that is used to adjust the initial position of the activator. It can be set to zero without loss of generality by assuming that one of the filament ends can be rotated arbitrarily. Therefore, for the rest of our analysis, we set $\theta_0 = 0$.

In order to understand the possible material and activation controls, we consider two extreme cases.

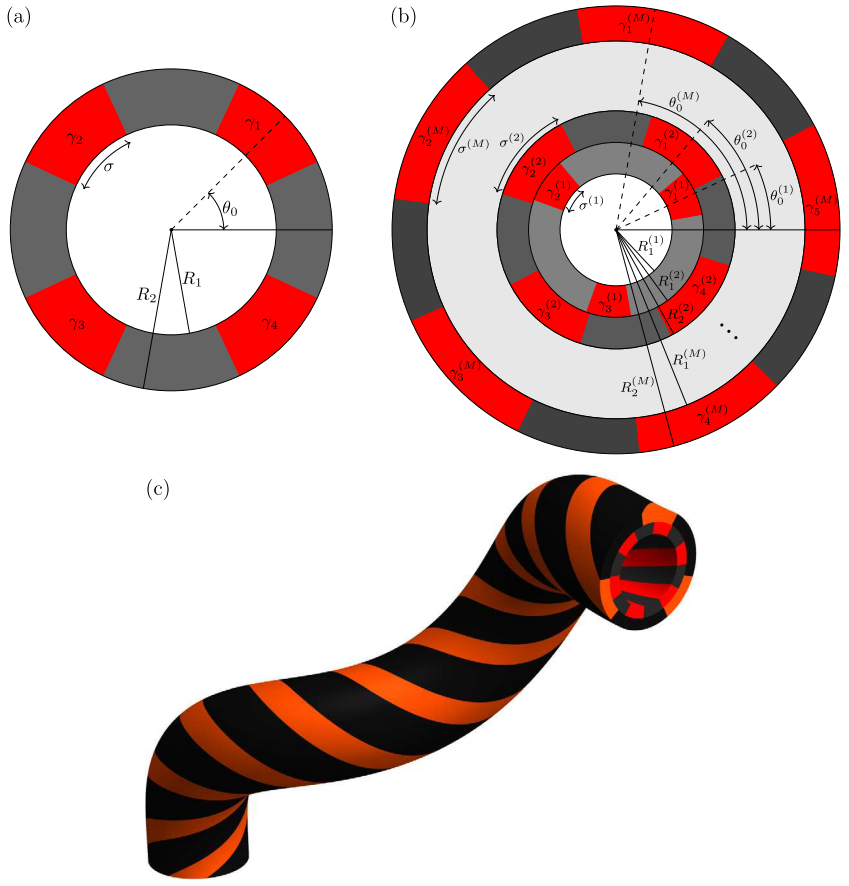

Fig. 4. Schematic representation of piecewise constant activation distributions $\gamma(\theta)$ for the case of a single-ring geometry (a), and a geometry with M concentric rings (b). Red-filled regions correspond to $\gamma \neq 0$, while all other regions are not activated. (c) A representative three-dimensional structure of an activated filament showing how the active regions twine around the main axis based on the angle of the fibers.

3.2.1. Curvature without torsion

We first look at the possibility of creating intrinsic curvature with helical fibers ($\alpha_2 \neq 0$) without intrinsic torsion. From the relation (57), we see that it requires a combination of material properties and activation. Indeed, δ_3 has the same sign as $\tan\alpha_2$. Hence, zero torsion can only occur if a_0 is negative, which implies contraction on average, and requires

$$a_0 = -\frac{R_0^3}{2\delta_3}\tan\alpha_2. \tag{62}$$

In addition, we need $A = \sqrt{a_1^2 + b_1^2}$ to be non-vanishing, which implies that all the γ_i cannot be equal to each other. We show in Fig. 5 that zero torsion is only possible for small values of the helical angle, as higher values would require unrealistically large values of $-\gamma_i$.

3.2.2. Twist without curvature

In the absence of curvature, there can be no torsion. Thus, the complementary problem to the problem of curvature without torsion is twisting a rod in the absence of curvature. There are two ways that can be used to remove curvature from the system.

First, by symmetry, we have that $a_1 = b_1 = 0$ if $\gamma_i = \gamma$ for all i. In this case, the system does not develop any curvature but only twist.

Second, we can design the structure so that $\delta_1 = 0$ for all activations. Indeed for given radii R_1 and $R_2 = R_0$, we can choose the angle α_2 so that $\delta_1 = 0$ as shown in Fig. 6. This can only happen for a narrow range of angles between $\alpha_2^* \leq \alpha_2 \leq \alpha_2^{**}$, where $\alpha_2^* = \arccos(-1/3)/2$ is the magic angle and α_2^{**} is the solution of $1 = -9\alpha_2\cot^3\alpha_2 + 9\cot^2\alpha_2$.

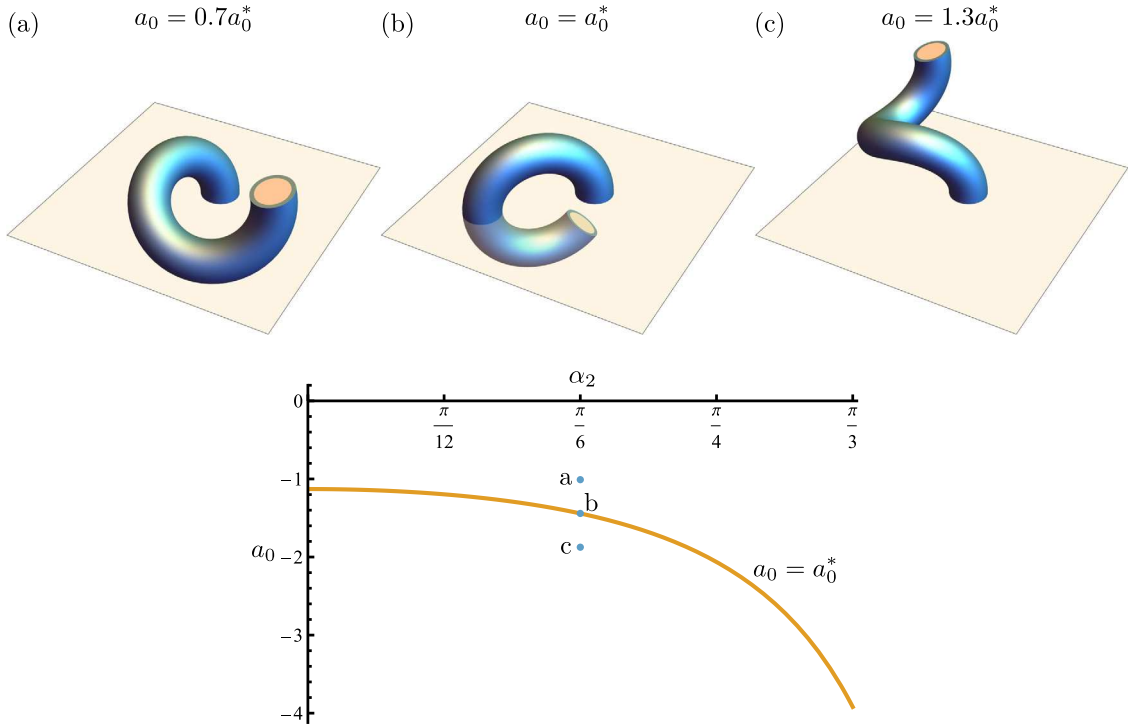

Fig. 5. Deformed configurations for three different values of a_0: (a) $a_0 = 0.7a_0^*$ below the threshold value $a_0^* \approx -1.44$, (b) a_0 equal to the threshold value a_0^*, (c) $a_0 = 1.3a_0^*$ above the threshold value a_0^*. Computations assumed $\alpha_2 = \pi/6$, $R_1 = 0.8$, $R_2 = R_0 = 1.0$, $L = 20$, $E = 1$, $\nu = 1/2$, and $a_1 = b_1 = 0.45$. The three configurations are mapped to their corresponding points on the plot of a_0 vs. α_2. Configuration (b) exhibits zero torsion and non-zero curvature, and its respective point in the (α_2, a_0) plane coincides with the threshold curve $a_0 = a_0^*$.

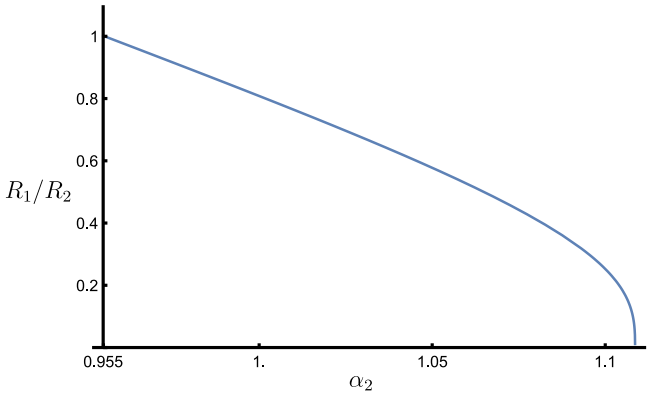

Fig. 6. Values of R_1/R_2 as a function of the helical angle α_2 leading to twist but no curvature. Here, $R_2 = R_0$, $\nu = 1/2$.

4. Multiple rings

We can design a filamentary structure with multiple rings as shown in Fig. 4. In this case, each new ring contributes to the intrinsic curvatures additively. Denoting by a superscript $(\,)^{(i)}$ a quantity attached to the ith ring from 1 to M, we simply have:

$$\hat{\zeta} = 1 + \frac{1}{2R_0^2} \sum_{i=1}^{M} a_0^{(i)} \delta_0^{(i)}, \tag{63}$$

$$\hat{u}_1 = -\frac{4}{3R_0^4} \sum_{i=1}^{M} A^{(i)} \delta_1^{(i)} \sin(\varphi^{(i)} - \frac{Z}{R_2^{(i)}} \tan \alpha_2^{(i)}), \tag{64}$$

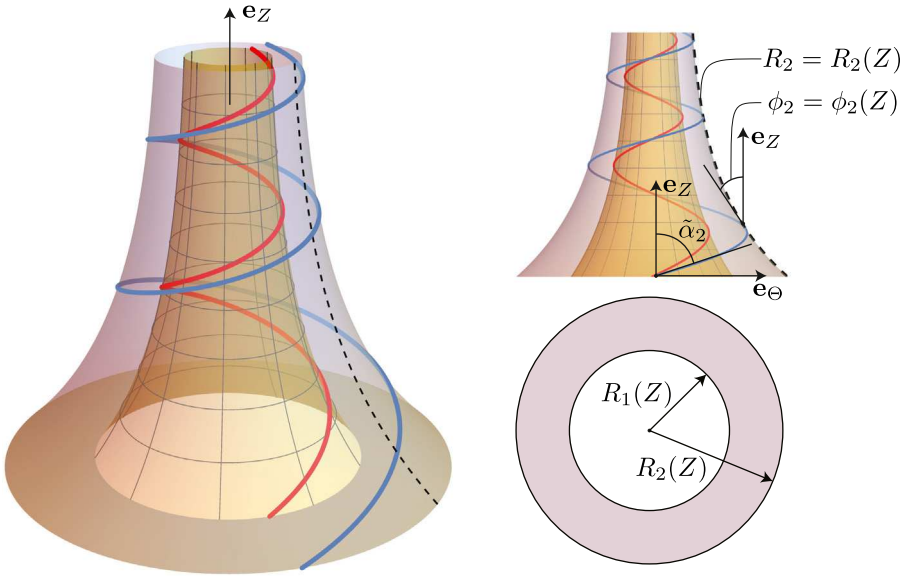

Fig. 7. Domain geometry and helical fiber architecture in the tapered filament case: a three-dimensional view (left), an orthographic side view (top-right), and a cross-sectional slice (bottom-right). Representative fibers are shown on two surfaces of revolution $R = R_2(Z)$, $R = R_1(0)R_2(Z)/R_2(0)$, where $R_2(Z) = R_2(0)f(Z)$ is some arbitrary tapering profile. On $R = R_2(Z)$, $\tilde{\alpha}_2$ is constant by construction, while the tapering angle on $R = R_2$, i.e. ϕ_2, is a function of Z for a general $R_2(Z)$.

$$\hat{u}_2 = -\frac{4}{3R_0^4}\sum_{i=1}^{M} A^{(i)}\delta_1^{(i)}\cos(\varphi^{(i)} - \frac{Z}{R_2^{(i)}}\tan\alpha_2^{(i)}), \tag{65}$$

$$\hat{u}_3 = \frac{2}{R_0^4}\sum_{i=1}^{M}\delta_3^{(i)}a_0^{(i)}, \tag{66}$$

where the expressions for $\delta_0^{(i)}$, $\delta_1^{(i)}$, $\delta_3^{(i)}$ are obtained by replacing R_1 and R_2 by the internal and external radii of the ith ring $R_1^{(i)}$ and $R_2^{(i)}$, respectively.

For these solutions, unless the helical angles follow the same rule (42) in all rings, the curvature and torsion are not constant anymore and the activation induces therefore non-helical solutions that can be controlled through the activation parameters. The space of solutions becomes quite rich even with two rings, as demonstrated in Fig. 4. However, a difficulty arises here in that the space of potential configurations cannot be easily quantified, since the actual position of the rod's centerline in space, $\mathbf{r}(Z)$, is difficult to describe as a function of activation.

5. Tapered filaments

Many filamentary structures are tapered. It is therefore of interest to understand the advantages or differences that these structures present with respect to a simpler cylindrical profile. The tapering is characterized by a function $f = f(Z)$ with $f(0) = 1$ such that the external and internal radii are given by $R_2(Z) = R_2(0)f(Z)$, and $R_1(Z) = R_1(0)f(Z)$, respectively. At a point Z, the graph of the function $R_2(Z)$ makes an angle $\phi_2(Z)$ with the Z-axis as shown in Fig. 7, while $\phi = \phi(R, Z)$ is the general fiber tapering angle which varies in both R and Z, such that $\phi_2(Z) = \phi(R_2, Z)$. We want to define local angles for the fiber $\mathbf{m}$ on the surface that have the same interpretation as in the case of untapered filaments. To do so, we introduce the local angles $\tilde{\alpha}$ and $\tilde{\beta}$, and a rotation matrix

$$\mathbf{R} = \begin{bmatrix} \cos\phi & 0 & -\sin\phi \\ 0 & 1 & 0 \\ \sin\phi & 0 & \cos\phi \end{bmatrix}. \tag{67}$$

A fiber defined by a vector

$$\tilde{\mathbf{m}} = \sin\tilde{\alpha}\sin\tilde{\beta}\,\mathbf{e}_R + \sin\tilde{\alpha}\cos\tilde{\beta}\,\mathbf{e}_\Theta + \cos\tilde{\alpha}\,\mathbf{e}_Z, \quad \tilde{\alpha}, \tilde{\beta} \in]-\pi/2, +\pi/2] \tag{68}$$

is mapped to

$$\begin{aligned}\mathbf{m} &= \mathbf{R}\cdot\tilde{\mathbf{m}} \\ &= (\sin\tilde{\alpha}\sin\tilde{\beta}\cos\phi - \cos\tilde{\alpha}\sin\phi)\,\mathbf{e}_R + \sin\tilde{\alpha}\cos\tilde{\beta}\,\mathbf{e}_\Theta + (\sin\tilde{\alpha}\sin\tilde{\beta}\sin\phi + \cos\tilde{\alpha}\cos\phi)\,\mathbf{e}_Z.\end{aligned} \tag{69}$$

These angles now have the same interpretation as the ones given in Fig. 3. For instance, an axial fiber in the tapered case lies in a plane that contains the Z-axis and is characterized by $\tilde{\alpha} = \tilde{\beta} = 0$, and so on. Using these new angles, we can compute the two angular functions that enter the active filament formulas:

$$\cos 2\alpha = \sin 2\tilde{\alpha} \sin \tilde{\beta} \sin 2\phi - \sin^2 \tilde{\alpha} \left(\sin^2 \tilde{\beta} \cos 2\phi + \cos^2 \tilde{\beta}\right) + \cos^2 \tilde{\alpha} \cos 2\phi, \tag{70}$$

$$\cos \beta \sin 2\alpha = 2 \sin \tilde{\alpha} \cos \tilde{\beta} \left(\sin \tilde{\alpha} \sin \tilde{\beta} \sin \phi + \cos \tilde{\alpha} \cos \phi\right). \tag{71}$$

5.1. Curvature and torsion in tapered filaments

In the case of the ring solution, we utilize a uniform twist relationship for the tapered fiber field akin to (42), such that

$$\frac{\tan \tilde{\alpha}}{R} = \frac{\tan \tilde{\alpha}_2}{R_2} = c_{\tilde{\alpha}}, \quad \frac{\tan \phi}{R} = \frac{\tan \phi_2}{R_2} = c_{\phi}, \tag{72}$$

where $c_{\tilde{\alpha}} = c_{\tilde{\alpha}}(Z)$, $c_{\phi} = c_{\phi}(Z)$ are introduced for notational brevity. For such a construction of a tapered fiber field, the activation function g can be written as $g(R, \Theta) = \gamma(\Theta - \tilde{\Theta})$, where the angular shift function $\tilde{\Theta}$ is given by

$$\tilde{\Theta}(R^0, Z) = \tan \tilde{\alpha}_2 \int_0^Z \frac{\sqrt{1 + \left[R^0 f'(s)\right]^2}}{R_2(0) f(s)} \, ds, \tag{73}$$

and $R^0 \in [R_1(0), R_2(0)]$ is the radius at which a given activated fiber originates at $Z = 0$. Under the assumption of a slow tapering profile $f(Z)$, the variation of $\tilde{\Theta}$ with respect to R^0 is negligible. Thus, we can perform the substitution $R^0 \leftarrow R_2(0)$ to obtain an approximate form $\tilde{\Theta}_2(Z) = \tilde{\Theta}(R_2(0), Z)$ of the angular shift, which depends only on Z. Then, substituting $g(R, \Theta) = \gamma(\Theta - \tilde{\Theta}_2)$ into (38)-(41) yields

$$H_0 = \frac{E\pi}{4} \delta_0 a_0, \tag{74}$$

$$H_1 = -\frac{E\pi}{6} \delta_1 A \sin(\varphi - \tilde{\Theta}_2), \tag{75}$$

$$H_2 = \frac{E\pi}{6} \delta_2 A \cos(\varphi - \tilde{\Theta}_2), \tag{76}$$

$$H_3 = \frac{E\pi}{6} \delta_3 a_0, \tag{77}$$

where δ_0, $\delta_1 = \delta_2$, δ_3 are functions of $c_{\tilde{\alpha}}$, $\tilde{\beta}$, c_{ϕ}, R_1, R_2, ν, and all other quantities are defined as before. In the case of tangentially helical fibers ($\tilde{\beta} = 0$), δ_i reduce to

$$\delta_0 = 2\left(R_1^2 - R_2^2\right)\nu - \frac{2(1+\nu)}{c_{\phi}^2 - c_{\tilde{\alpha}}^2} \log\left(\frac{\left(1 + R_1^2 c_{\phi}^2\right)\left(1 + R_2^2 c_{\tilde{\alpha}}^2\right)}{\left(1 + R_2^2 c_{\phi}^2\right)\left(1 + R_1^2 c_{\tilde{\alpha}}^2\right)}\right), \tag{78}$$

$$\delta_1 = \delta_2 = \frac{2}{c_{\phi} c_{\tilde{\alpha}} \left(c_{\phi}^2 - c_{\tilde{\alpha}}^2\right)} \Big[3(1+\nu)\left(\arctan\left(R_1 c_{\phi}\right) - \arctan\left(R_2 c_{\phi}\right)\right) c_{\tilde{\alpha}} + \left(R_1^3 - R_2^3\right) \nu c_{\phi}^3 c_{\tilde{\alpha}} - c_{\phi}\left(3(1+\nu)\left(\arctan\left(R_1 c_{\tilde{\alpha}}\right) - \arctan\left(R_2 c_{\tilde{\alpha}}\right)\right) + \left(R_1^3 - R_2^3\right)\nu c_{\tilde{\alpha}}^3\right)\Big], \tag{79}$$

$$\delta_3 = \frac{3}{c_{\phi}^2 c_{\tilde{\alpha}}^2 \sqrt{c_{\phi}^2 - c_{\tilde{\alpha}}^2}} \left[\left(T(-R_1) + T(R_1) - T(-R_2) - T(R_2)\right) c_{\phi}^2 + 2 c_{\tilde{\alpha}} \left(-S(R_1) + S(R_2)\right)\right], \tag{80}$$

where

$$T(R) = \arctan\left(\frac{c_{\tilde{\alpha}} + i c_{\phi}^2 R}{S(R)}\right), \quad S(R) = \sqrt{\left(c_{\phi}^2 - c_{\tilde{\alpha}}^2\right)\left(1 + c_{\phi}^2 R^2\right)}. \tag{81}$$

The intrinsic extension and curvatures are then obtained via (36).

Utilizing this result, we consider the intrinsic curvature, $\hat{\kappa}$, for axially tapered fibers ($\tilde{\alpha}_2 = 0$, $\tilde{\beta} = 0$), and torsion, $\hat{\tau}$, for helically tapered fibers ($\tilde{\alpha}_2 \neq 0$, $\tilde{\beta} = 0$). These quantities are computed for three different functional forms of the tapering profile $f(Z)$, as shown in Fig. 8. Consistently with intuition, both curvature and torsion are monotonically increasing functions of Z for all considered tapering profiles, as manifested by the spiraling shapes of the deformed filaments. Interestingly, for each of the three cases, the normalized curvature and torsion functions are approximately equal for Z outside of the close neighborhood of $Z = 0$; hence the collapse of $\hat{\kappa}/\hat{\kappa}_{\max}$ and $\hat{\tau}/\hat{\tau}_{\max}$ into one curve in each of the three plots. Further, the shapes of the normalized $\hat{\kappa}$ and $\hat{\tau}$ curves are not trivial despite the monotonicity of $f(Z)$ and its derivatives, as exemplified by the inflection point in the curvature and torsion functions for the logarithmic profile. Such a complexity arises primarily since we account for the activation of a tapered fiber field embedded in a tapered domain geometry. Such an approach is more biologically relevant because a non-tapered field contained in a tapered domain would result in premature termination of fibers inside the filament.

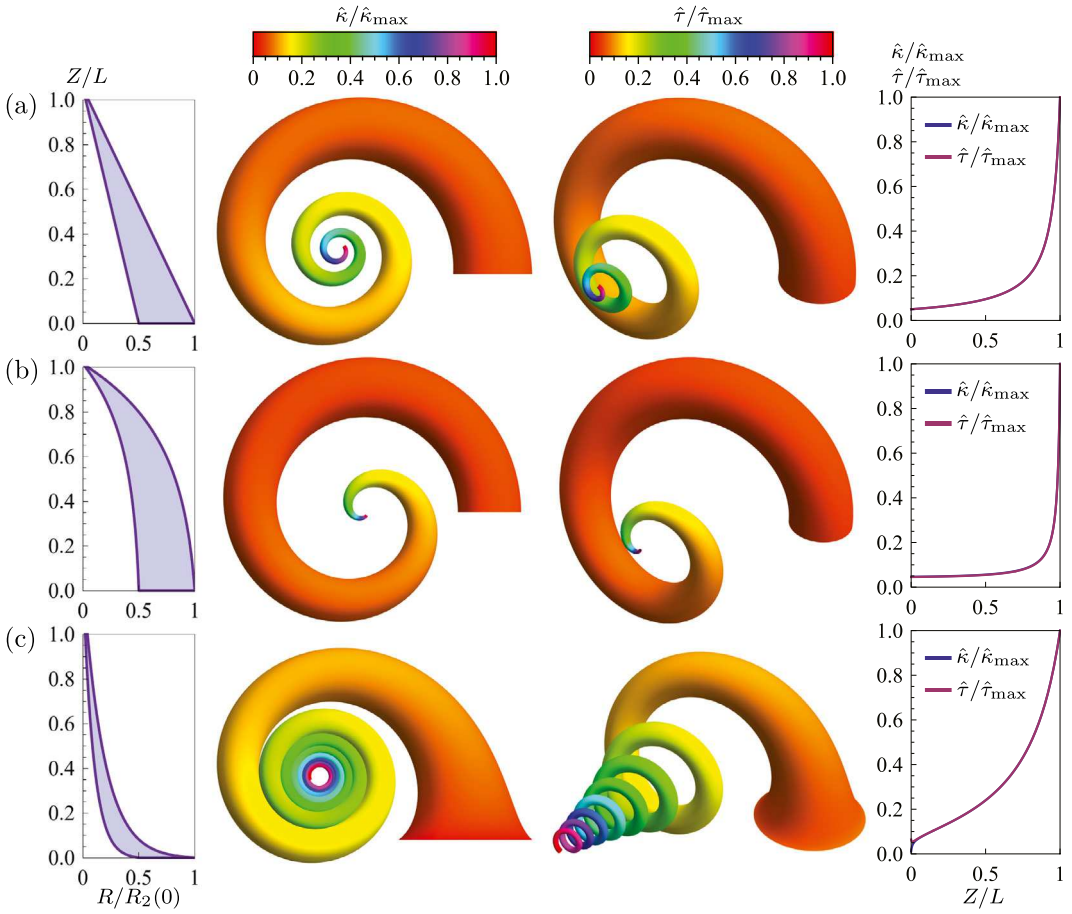

Fig. 8. Deformations of filaments with different tapering profiles (a, b, c) for both axial and helical fiber architectures. The first column shows the tapering profile geometry. The functional forms of the three profiles under consideration are: (a) linear $f(Z) = c_1 Z + c_2$, (b) exponential $f(Z) = c_1 + c_2 e^{c_3 Z}$, (c) logarithmic $f(Z) = c_1 \log(c_2 Z + c_3)$. The second and third columns show representative deformations of rods with axial fibers ($\tilde{\alpha}_2 = 0$, $\tilde{\beta} = 0$) and helical fibers ($\tilde{\alpha}_2 = \pi/64$, $\tilde{\beta} = 0$) respectively. The coloring of the rod surfaces corresponds to curvature (second column) and torsion (third column) normalized by their respective maximum values, for $Z \in [0, L]$. Plots of said normalized curvature and torsion functions are presented in the fourth column. All tapering profiles assumed $R_2(0)/R_1(0) = 2$, $L/R_2(0) = 25$, and all deformations were computed for $a_1 = 0.2$, $a_0 = b_1 = 0$, $E = 1$, $\nu = 0.5$.

5.2. Activation in non-tapered and tapered filaments

We now compile the main results to inform the comparison of configurations resulting from activation in non-tapered and tapered filaments. In particular, as shown in Fig. 9, we consider a multi-ring geometry in both cases. The first ring contains axial fibers ($\tilde{\alpha}^{(1)} = \tilde{\beta}^{(1)} = 0$), and the second ring consists of helical fibers ($\tilde{\alpha}^{(2)} \neq 0$, $\tilde{\beta}^{(2)} = 0$), with $\phi_2^{(i)} = 0$ and $\phi_2^{(i)} > 0$ in the non-tapered and tapered scenarios, respectively. In such a setup, the first ring enables direct curvature control, while the activation of the second ring promotes torsion. Generally, these effects are not decoupled when both rings are activated simultaneously, so special care needs to be taken in designing the activation patterns for a desired configuration to be attained.

The same activation distributions, $\gamma^{(1)}(\theta)$, $\gamma^{(2)}(\theta)$ (Fig. 9e), are prescribed in the corresponding rings in both geometries, for the comparison to be meaningful. Moreover, the initial ring thicknesses $R_2^{(i)}(0) - R_1^{(i)}(0)$ are set to be the same in both cases, so that the activation magnitudes are comparable as well. In order to ensure that the outer boundary of the first ring and the inner boundary of the second ring coincide at all Z, $\phi_2^{(1)}$ is chosen such that $R_2^{(1)}(0) = R_1^{(2)}(0)$ and $c_\phi^{(1)} = c_\phi^{(2)}$ at all Z, for some $\phi_2^{(2)}$. For simplicity, the tapering profile $f(Z)$ is chosen to be linear, but the same analysis can be readily applied for an arbitrary form of $f(Z)$.

Activation of the tapered filament (Fig. 9g) results in a notably more elaborate configuration, as compared to the deformed shape of the non-tapered geometry (Fig. 9f). The variation in the magnitude of curvature and torsion is considerably larger in the tapered case, as expected based on the prior analysis in Fig. 8, but it is now confirmed for the multi-ring scenario. Further, the tapered configuration is more compact in space due to the same activation magnitudes being applied in rings of decreasing thickness, which induces significant curvature and torsion especially towards the end of the filament.

From a practical perspective, the tapered filament assumes a morphology similar to a biological arm during a grappling motion, such as an elephant trunk wrapping around a tree branch. The development of a physiologically functional configuration upon activation in the tapered case might point to the mechanical role of tapering in biological filaments.

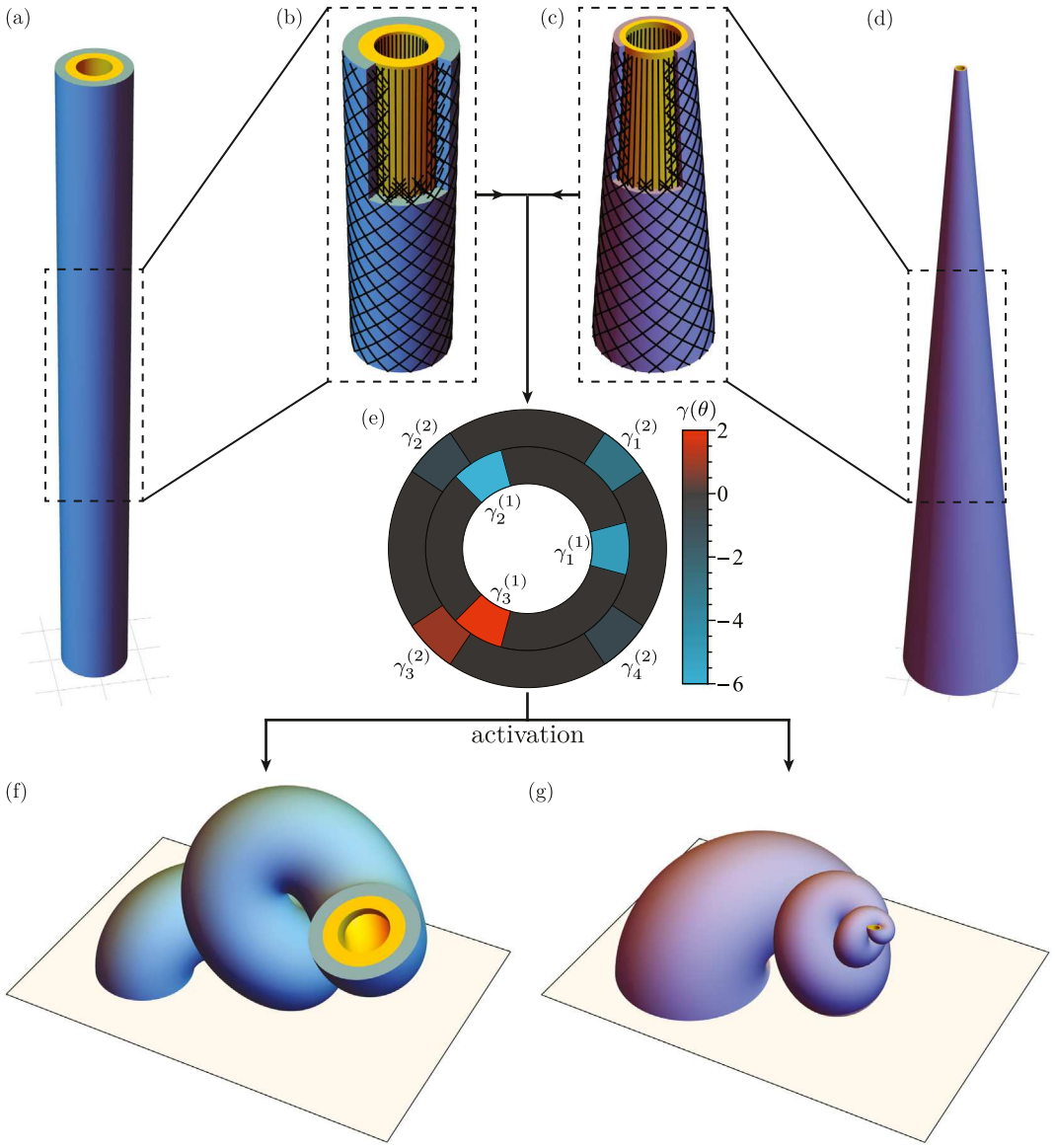

Fig. 9. Comparison of configurations developed upon activation in the non-tapered and tapered cases. A multi-ring geometry with rings of equal thickness is assumed in both (a) the non-tapered reference configuration, and (d) the tapered reference configuration. (b), (c) Both domains contain axial fibers embedded in the first ring and helical fibers in the second ring. (e) The same activation distributions $\gamma^{(1)}(\theta)$, $\gamma^{(2)}(\theta)$ are simulated in both the non-tapered and tapered scenarios. Imposing the activation results in configurations (f) and (g) for the non-tapered and tapered cases, respectively. Parameters for the non-tapered reference geometry: $R_1^{(1)} = 0.7$, $R_1^{(2)} = R_2^{(1)} = 1.1$, $R_2^{(2)} = 1.5$, $L = 30$, $\alpha_2^{(2)} = \pi/4$, $\alpha_2^{(1)} = \beta^{(1)} = \beta^{(2)} = 0$; for the tapered reference geometry: $R_1^{(1)}(0) = 1.8$, $R_1^{(2)}(0) = R_2^{(1)}(0) = 2.2$, $R_2^{(2)}(0) = 2.6$, $L = 30$, $\tilde{\alpha}_2^{(2)} = \pi/4$, $\phi_2^{(2)} = \pi/40$, $\tilde{\alpha}_2^{(1)} = \tilde{\beta}^{(1)} = \tilde{\beta}^{(2)} = 0$. Material parameters were chosen to be $E = 1$, $\nu = 0.5$ in both cases.

6. Conclusion

Active filaments are one-dimensional structures that remodel internally. Here, we have assumed that the lone source of this remodeling process is a fiber activation field given at any point in the material, specifying extension or contraction in a given direction. The case of activation by growth or muscular contraction are both taken into account through the specification of a Poisson-like ratio for the extending fiber. This fiber activation is not the most general case of activation as, in principle, a full anelastic tensor could be specified at each point. Yet, from a modeling point of view, these fiber-driven active structures are ubiquitous and universal. Within this framework, we derived the so-called *active filament formulas* linking fiber stretch and orientation to the intrinsic curvatures generated by the remodeling process.

We further restricted our attention to the case of filaments with circular cross sections and ring solutions for rope-like structures. In these materials, the orientation of the fiber is slaved to the orientation of the active material. As the active material coils around

the central core, we assume that the activation takes place in the tangential direction to the coil. A mathematically pleasing model for these structures is given by ring solutions with well-defined sectors of activation, each specified by a single angle, hence restricting the number of parameters. In this case, further analytical progress leads to an explicit form of the curvatures in terms of the Fourier decomposition of the activation functions. The sets of possible shapes of these structures, even in the simple case of a single active ring with a finite number of activation sectors, are remarkably rich. In particular, we showed that a chiral helically-wrapped filament can be tuned to create an achiral intrinsic shape with curvature but no torsion, or a structure with twist but without curvature. It is straightforward to consider these interesting limiting cases, since most of the derived expressions have an analytic form.

From an engineering perspective, the case of curvature without torsion corresponds to the typical application in metallic bi-layer actuators. The possibility that one can also achieve twisting without curvature is more surprising, and it constitutes a type of actuation that could be of potential interest to the soft-robotics community.

Our analysis is limited to filaments that are initially straight. If the initial curvature is relatively small with respect to the length, we expect that the intrinsic curvature will be the sum of the initial curvature and the curvature induced by activation. However, for larger curvature, the analysis should be done properly, e.g., starting with a ring or helical initial configuration.

We generalized the ring solutions to the case of tapered filaments, another ubiquitous feature of the natural world. We showed that for a given tapering function, intrinsic curvatures can still be obtained, albeit at the expense of increasingly more complicated analytical formulas. Tapering provides yet another opportunity for control, especially in its ability to create large curvature at the small end of the filament. One would naturally expect that the intrinsic curvature increases as the radius decreases and, once the internal balance of forces is computed, this is mostly what we observe. Yet, the change in radius R has another important effect, as it changes the stiffness of the structure. The typical scaling for the bending stiffness, inherited from the second moment of area, is R^4. Hence, the tapering not only affects the curvature, but also allows to connect a stiff region (large radii), that needs to support the weight of the filament, to a soft region (small radii) dedicated to fine manipulations. This is exactly what is observed in the massive elephant trunk in the animal kingdom.

The framework presented here provides a general analytical formulation for the problem of active filaments. It can now be adapted for specific challenges in physics and engineering — particularly, solving inverse problems found in robotics, where a given geometrical property or a final shape of a soft-robotic filament is sought, and the activation functions need to be determined. It can also be used to understand typical and universal design of natural manipulators, such as the elephant trunk.

Declaration of competing interest

The authors declare that they have no known competing financial interests or personal relationships that could have appeared to influence the work reported in this paper.

Acknowledgments

This work was supported by the Burt and Deedee McMurtry Stanford Graduate Fellowship in Science & Engineering to B.K. The support for A.G. by the Engineering and Physical Sciences Research Council of Great Britain under research grant EP/R020205/1 is gratefully acknowledged. E.K. was supported by the National Science Foundation grant CMMI 1727268.

References

Antman, S.S., 2005. Nonlinear Problems of Elasticity. Springer, New York.
Audoly, Basile, Lestringant, Claire, 2021. Asymptotic derivation of high-order rod models from non-linear 3D elasticity. J. Mech. Phys. Solids 148, 104264.
Bauer, Robert, Neukamm, Stefan, Schäffner, Mathias, 2019. Derivation of a homogenized bending–torsion theory for rods with micro-heterogeneous prestrain. arXiv preprint arXiv:1903.08290.
Benham, C.J., 1979. An elastic model of the large structure of duplex DNA. Bioploymers 18, 609–623.
Beveridge, D.L., Barreiro, G., Byun, K.S., Case, D.A., Cheatham, T.E., Dixit, S.B., Giudice, E., Lankas, F., Lavery, R., Maddocks, J.H., et al., 2004. Molecular dynamics simulations of the 136 unique tetranucleotide sequences of DNA oligonucleotides. I. research design and results on d (c p g) steps. Biophys. J. 87 (6), 3799–3813.
Brun, Pierre-Thomas, Ribe, Neil, Audoly, Basile, 2014. An introduction to the mechanics of the lasso. Proc. Royal Soc. A: Math. Phys. Eng. Sci. 470 (2171), 20140512.
Calisti, M., Giorelli, M., Levy, G., Mazzolai, B., Hochner, B., Laschi, C., Dario, P., 2011. An octopus-bioinspired solution to movement and manipulation for soft robots. Bioinspiration Biomim. 6 (3), 036002.
Cicalese, Marco, Ruf, Matthias, Solombrino, Francesco, 2017. On global and local minimizers of prestrained thin elastic rods. Calc. Var. Partial Differential Equations 56 (4), 115.
Cimetière, Alain, Geymonat, Giuseppe, Dret, Herve Le, Raoult, Annie, Tutek, Zvonimir, 1988. Asymptotic theory and analysis for displacements and stress distribution in nonlinear elastic straight slender rods. J. Elasticity 19 (2), 111–161.
Costello, G.A., 1990. Theory of Wire Rope. Springer Verlag, New York.
de Payrebrune, Kristin M., O'Reilly, Oliver M., 2016. On constitutive relations for a rod-based model of a pneu-net bending actuator. Extreme Mech. Lett. 8, 38–46.
Dill, E.H., 1992. Kirchhoff's theory of rods. Arch. Hist. Exact. Sci. 44, 2–23.
Goldstein, R.E., Goriely, A., 2006. Dynamic buckling of morphoelastic filaments. Phys. Rev. E 74, 010901.
Goriely, A., 2017. The Mathematics and Mechanics of Biological Growth. Springer Verlag, New York.
Goriely, A., Maddocks, J.H., Durickovic, B., 2012. Twist and stretch of helices: All you need is love. Preprint.
Goriely, A., Moulton, D.E., 2010. Morphoelasticity - A theory of elastic growth. In: New Trends in the Physics and Mechanics of Biological Systems. Oxford University Press.
Goriely, Alain, Moulton, Derek E., Angela Mihai, L., 2022. A rod theory for liquid crystalline elastomers. J. Elast.

Goriely, A., Neukirch, S., 2006. Mechanics of climbing and attachment in twining plants. Phys. Rev. Lett. 97 (18), 184302.
Goriely, A., Tabor, M., 1998. Spontaneous helix-hand reversal and tendril perversion in climbing plants. Phys. Rev. Lett. 80, 1564–1567.
Goriely, A., Tabor, M., 2000. The nonlinear dynamics of filaments. Nonlinear Dynam. 21 (1), 101–133.
Goriely, A., Tabor, M., 2013. Rotation, inversion and perversion in anisotropic elastic cylindrical tubes and membranes. Proc. Roy. Soc. Lond. A 469, 2153.
Greenhill, A.G., 1881. Determination of the greatest height consistent with stability that a vertical pole or mast can be made, and of the greatest height to which a tree of given proportions can grow. Pro. Cambridge Philos. Soc. 4 (part 2), 65–73.
Guillon, T., Dumont, Y., Fourcaud, T., 2011. A new mathematical framework for modelling the biomechanics of growing trees with rod theory. Math. Comput. Model. 55, 2061–2077.
Hannan, Michael W., Walker, Ian D., 2003. Kinematics and the implementation of an elephant's trunk manipulator and other continuum style robots. J. Robot. Syst. 20 (2), 45–63.
Hoffman, K.A., Manning, R.S., Maddocks, J.H., 2003. Link, twist, energy, and the stability of DNA minicircles. Biopolymers 70, 145–157.
Hofhuis, H., Moulton, D., Lessinnes, T., Routier-Kierzkowska, A.-L., Bomphrey, R.J., Mosca, G., Reinhardt, H., Sarchet, P., Gan, X., Tsiantis, M., Ventikos, Y., Walker, S., Goriely, A., Smith, R., Hay, A., 2016. Morphomechanical innovation drives explosive seed dispersal. Cell 166, 222–233.
Jones, Trevor J., Jambon-Puillet, Etienne, Marthelot, Joel, Brun, P.-T., 2021. Bubble casting soft robotics. Nature 599 (7884), 229–233.
Kier, W.M., 2012. The diversity of hydrostatic skeletons. J. Exp. Biol. 215 (8), 1247–1257.
Kier, W.M., Smith, K.K., 1985. Tongues, tentacles and trunks: The biomechanics of movement in muscular-hydrostats. Zool. J. Linn. Soc. 83 (4), 307–324.
Kirchhoff, G., 1859. Über das gleichgewicht und die bewegung eines unendlich dünnen elastischen stabes. J. Reine Angew. Math. 56, 285–313.
Kohn, Robert V., O'Brien, Ethan, 2018. On the bending and twisting of rods with misfit. J. Elast. 130 (1), 115–143.
Kupferman, Raz., Solomon, Jake P., 2014. A Riemannian approach to reduced plate, shell, and rod theories. J. Funct. Anal. 266 (5), 2989–3039.
Laschi, Cecilia, Cianchetti, Matteo, Mazzolai, Barbara, Margheri, Laura, Follador, Maurizio, Dario, Paolo, 2012. Soft robot arm inspired by the octopus. Adv. Robot. 26 (7), 709–727.
Lessinnes, Th., Moulton, D.E., Goriely, A., 2017. Morphoelastic rods. Part II: Growing birods. J. Mech. Phys. Solids 100, 147–196.
Levinson, Yaron, Segev, Reuven, 2010. On the kinematics of the octopus's arm. J. Mech. Robot. 2 (1), 011008.
McMillen, T., Goriely, A., 2002. Whip waves. Physica D 184.
McMillen, T., Holmes, P., 2006. An elastic rod model for anguilliform swimming. J. Math. Biol. 53 (5), 843–886.
Mora, Maria Giovanna, Müller, Stefan, 2003. Derivation of the nonlinear bending-torsion theory for inextensible rods by Γ-convergence. Calc. Var. Partial Differential Equations 18 (3), 287–305.
Moulton, D.E., Lessinnes, T., Goriely, A., 2012. Morphoelastic rods part I: A single growing elastic rod. J. Mech. Phys. Solids 61 (2), 398–427.
Moulton, Derek E., Lessinnes, Thomas, Goriely, Alain, 2020a. Morphoelastic rods III: Differential growth and curvature generation in elastic filaments. J. Mech. Phys. Solids 104022.
Moulton, D.E., Lessinnes, T., O'Keeffe, S., Dorfmann, L.A., Goriely, A., 2016. The elastic secrets of the chameleon tongue. Proc. Roy. Soc. Lond. A 472 (2188), 20160030.
Moulton, Derek E., Oliveri, Hadrien, Goriely, Alain, 2020b. Multiscale integration of environmental stimuli in plant tropism produces complex behaviors. Proc. Natl. Acad. Sci. 117 (51), 32226–32237.
Neukirch, S., Goriely, A., Hausrath, A.C., 2008a. Chirality of coiled coils: Elasticity matters. Phys. Rev. Lett. 100 (3), 038105.
Neukirch, S., Goriely, A., Hausrath, A.C., 2008b. Elastic coiled-coils act as energy buffers in the ATP synthase. Int. J. Nonlinear Mech. 43, 1064–1073.
Oliveri, Hadrien, Franze, Kristian, Goriely, Alain, 2021. Theory for durotactic axon guidance. Phys. Rev. Lett. 126 (11), 118101.
Paley, Derek A., Wereley, Norman M., 2021. Bioinspired Sensing, Actuation, and Control in Underwater Soft Robotic Systems. Springer.
Sanchez-Hubert, Jacqueline, Palencia, Evarisre Sanchez, 1999. Statics of curved rods on account of torsion and flexion. Eur. J. Mech. A Solids 18 (3), 365–390.
Sano, Tomohiko G., Pezzulla, Matteo, Reis, Pedro M., 2021. A Kirchhoff-like theory for hard magnetic rods under geometrically nonlinear deformation in three dimensions. arXiv preprint arXiv:2106.15189.
Sheley, M.J., Ueda, T., 2000. The Stokesian hydrodynamics of flexing, stretching filaments. Phytsica D 146.
Shoshani, Jeheskel, 1998. Understanding proboscidean evolution: A formidable task. Trends Ecol. Evol. 13 (12), 480–487.
Thomson, W.T., Tait, P.G., 1867. Treatise on Natural Philosophy. Cambridge.
Walker, Ian D., Dawson, Darren M., Flash, Tamar, Grasso, Frank W., Hanlon, Roger T., Hochner, Binyamin, Kier, William M., Pagano, Christopher C., Rahn, Christopher D., Zhang, Qiming M., 2005. Continuum robot arms inspired by cephalopods. In: Unmanned Ground Vehicle Technology VII, Vol. 5804. International Society for Optics and Photonics, pp. 303–314.
Wilson, J.F., Mahajan, U., Wainwright, S.A., Croner, L.J., 1991. A continuum model of elephant trunks. J. Biomech. Eng. 113 (1), 79–84.
Yokota, J.W., Bekele, S.A., Steigmann, D.J., 2001. Simulating the nonlinear dynamics of an elastic cable. AIAA J. 39 (3), 504–510.